ADVANCED FUNCTIONAL MATERIALS
www.afm-journal.de

Single Atom-Particle Tandem Catalysis Enables Enhanced Desolvation Kinetics for Low-Temperature Li-S Batteries

Yuhang Lin, Jian Wang, Xin Zhang, Xiaomin Cheng, Quan Zhuang, Jing Zhang, Qinghua Guan, Yanli Wang,* Chunyin Shen, Hongzhen Lin, Liang Zhan,* Licheng Ling, and Yongzheng Zhang**

The commercial implementation of lithium-sulfur (Li-S) batteries is plagued by the sluggish kinetics of interfacial Li(solvent)$_x^+$ desolvation and successive redox conversions of sulfur species, exhibiting high tandem barriers. Herein, the tandem catalyst consisted of single Fe atom and Fe_3C nanoparticles on porous carbon sheet (SAPTC@PCS) is initially proposed and developed. As illustrated in theoretical simulation, the neighboring Fe_3C further tunes the electronic density and affects related coordination structure of atomically distributed iron for reinforcing catalytic efficiency. The as-prepared SAPTC@PCS facilitates the dissociation of Li(solvent)$_x^+$ to release more isolated Li^+ to participate in the subsequent polysulfide redox conversions by decreasing the desolvation/diffusion barriers, as revealed by in-situ Raman, time-of-flight second ion mass spectroscopy, electronic microscope and X-ray measurements. Consequently, the cell with SAPTC@PCS delivers a high capacity-retention over 1000 cycles and high rate up to 3 C. Impressively, under the practical mass loading of 6 mg cm^{-2}, the cell stabilizes the capacity of 4.59 mAh cm^{-2} after 90 cycles, and a desirable capacity of 804.8 mAh g^{-1} after 100 cycles is achieved even being exposed to low temperature of 0 °C, demonstrating the feasibility of single atom-particle catalysts for tandem catalysis in Li-S batteries.

1. Introduction

Lithium-sulfur (Li-S) batteries have attracted intensive attention due to their high theoretical capacity of 1675 mAh g^{-1}, environmental compatibility, and low cost.[1–4] However, the sluggish kinetics of interfacial Li(solvent)$_x^+$ desolvation and successive redox conversions of lithium polysulfides (LiPSs) impede their utilization and wide applications, especially under harsh conditions such as high mass loading and low-temperature operation.[5–7] In principal, the Li(solvents)$_x^+$ clusters in the electrolyte should be regulated to generate isolated Li^+ across the electrolyte/cathode interface to cathode bulk interior before reacting with sulfur species.[8–10] Regrettably, the large size Li(solvent)$_x^+$ clusters undertake huge diffusion barriers due to the steric hindrance effects, and require additional energy to break down internal coordination bonds of Li-solvents, leading to poor Li^+ transport

Y. Lin, X. Zhang, Y. Wang, C. Shen, L. Zhan, L. Ling, Y. Zhang
State Key Laboratory of Green Chemical Engineering and Industrial Catalysis
Key Laboratory of Specially Functional Polymeric Materials and Related Technology (Ministry of Education)
Shanghai Key Laboratory of Multiphase Materials Chemical Engineering
State Key Laboratory of Chemical Engineering
East China University of Science and Technology
130 Meilong Road, Shanghai 200237, China
E-mail: ylwang@ecust.edu.cn; zhanliang@ecust.edu.cn; zhangyongzheng@ecust.edu.cn

The ORCID identification number(s) for the author(s) of this article can be found under https://doi.org/10.1002/adfm.202501496

DOI: 10.1002/adfm.202501496

J. Wang, X. Cheng, Q. Guan, H. Lin
i-Lab & CAS Key Laboratory of Nanophotonic Materials and Device
Suzhou Institute of Nano-Tech and Nano-Bionics
Chinese Academy of Sciences
Suzhou, Jiangsu 215123, China
E-mail: wangjian2014@sinano.ac.cn, jian.wang@kit.edu

J. Wang
Helmholtz Institute Ulm (HIU)
D89081 Ulm, Germany

J. Wang
Karlsruhe Institute of Technology (KIT)
D76021 Karlsruhe, Germany

Q. Zhuang
Inner Mongolia Key Laboratory of Carbon Nanomaterials
Nano Innovation Institute (NII)
Inner Mongolia Minzu University
Tongliao 028000, China

J. Zhang
School of Materials Science and Engineering
Xi'an University of Technology
Xi'an 710048, China

and dissatisfactory sulfur conversions in the low-temperature surroundings.[11–13]

To address above tough issues, current conventional strategies focus on directly improving the utilization of sulfur species by constructing high conductive hosts/matrices or inducing strong absorbability toward LiPSs.[14–17] However, as mentioned above, the desolvation behavior of Li(solvents)$_x^+$ clusters is the prerequisite for polysulfide reactions, which is normally neglected by most researchers. Although the success in the decoration of porous materials such as metal organic frameworks and covalent organic frameworks for physically sieving large size Li(solvents)$_x^+$ clusters, the sieving effect is still far behind the demand of rapidly generating more bare Li^+ for reaction. The strategy of electrocatalysis is proposed to stimulate the dissociation kinetics of Li(solvent)$_x^+$ in a more efficient manner. For example, our group put forward a combined strategy of electrocatalysis and pore sieving effect to directly decompose the large size Li(solvents)$_x^+$ clusters to release abundant free Li^+ with a rapid diffusion kinetics through a nitrogen-doped carbon grafted CoP structure.[18] However, the agglomeration of the CoP nanoparticles would degrade the electrocatalysis and sieving efficiency for accelerating Li(solvents)$_x^+$ desolvation in the low-temperature surroundings.

Single-atom catalysts (SACs) attract our attention due to ideal atomic efficiency (100 at%) and the highly exposed active sites.[19–22] Among them, single atomic Fe active sites featuring Fe-N_4 configuration exhibit high intrinsic electrocatalytic activity to sulfur redox reactions, where the π-conjugated framework provides delocalized electrons. However, their catalytic capability is limited by the insufficient interaction among individual Fe-N_4 active site, which is not conducive to achieve optimal catalytic performance without external modulation. Increasing attention has been paid to regulate and disturb the local electronic structure of Fe-N_4 to achieve higher catalytic efficiency such as forming Fe-N_3C.[23–26] It has been demonstrated that introducing atomic catalyst on the defect-rich compounds can trigger electron delocalization and redistribution, leading to higher charge density and thus enhancing the catalytic activity for reducing related energy barriers.[27] Meanwhile, as well known, the high surface polarity of metal-based compounds can provide strong chemical adsorption and *d-p* orbital hybridization to polysulfides for achieving high sulfur utilization. Based on these considerations, it is of great significance to spatially integrate Fe-N_4 with metal compounds in dealing with the catalytic Li(solvents)$_x^+$ desolvation. However, the catalytic studies of interfacial Li(solvents)$_x^+$ desolvation in Li-S batteries are still in its fancy and deserve deep understanding.

Herein, the single Fe atom and Fe_3C nanoparticles on porous carbon sheet (SAPTC@PCS) is initially proposed and developed, serving as the tandem catalyst for desolvation and redox reaction. Specifically, the neighboring Fe_3C further tunes the electronic density to disturb coordination structure of atomically distributed iron for reinforcing catalytic efficiency. Both theoretical simulation and in situ Raman, time-of-flight second ion mass spectroscopy, electronic microscope and X-ray measurements show that the as-prepared SAPTC@PCS facilitates the dissociation of Li(solvent)$_x^+$ to release more isolated Li^+ to participate in the subsequent polysulfide redox conversions by decreasing the related barriers. Consequently, the Li-S cell with SAPTC@PCS delivers a high capacity-retention over 1000 cycles and high rate up to 3 C. Impressively, under the practical mass loading of 6 mg cm^{-2}, the cell stabilizes the areal capacity of 4.59 mAh cm^{-2} after 90 cycles, and a desirable capacity of 804.8 mAh g^{-1} after 100 cycles is achieved even being exposed to low temperature of 0 °C, demonstrating the feasibility of single atom-particle catalysts for tandem catalysis in Li-S batteries.

2. Results and Discussion

As illustrated in **Figure 1A**, the SAPTC@PCS was synthesized through a simple solvothermal-pyrolysis method, where the Fe-N_4 configurations and Fe_3C nanoparticles are generated during pyrolysis process. For comparison, N-doped carbon matrix (NC), iron single atoms on N-doped carbon matrix (Fe-N-C@NC), Fe_3C with a lower proportion single Fe atom on porous carbon sheet (Fe_3C/Fe_{low}@PCS) and Fe_3C on porous carbon sheet (Fe_3C@PCS) were prepared. The scanning electron microscope (SEM) and transmission electron microscope (TEM) images indicate that SAPTC@PCS is composed of two-dimensional carbon matrix and uniformly dispersed Fe_3C with the size of ~40 nm (Figure 1B,C; Figure S1, Supporting Information). The high-resolution TEM (HR-TEM) image and corresponding inverse fast Fourier transformation (IFFT) image on the selected area display the lattice fringes with an interplanar spacing of 0.211 nm, which is attributed to the (211) facet of orthorhombic Fe_3C (Figure S2, Supporting Information), as confirmed by X-ray diffraction (XRD) with characteristic peaks of Fe_3C (PDF#35-0772) (FigureS3, Supporting Information).[28,29] Further, the atomic state of iron was subjected to the high-angle annular dark-field scanning TEM (HAADF-STEM), showcasing numerous isolated Fe atoms (labeled in red circles) homogenously dispersed adjacent with the Fe_3C (labeled in green circles) (Figure 1D), generating the atom-particle structure. Pore structure analysis reveals that SAPTC@PCS has a richer pore structure than NC, displaying larger specific surface area (182.9 vs 34.0 m^2 g^{-1}) (Figure S4, Supporting Information), hence providing more sites for adsorption.[30–32] Then, X-ray photoelectron spectroscopy (XPS) was applied to study the surface chemical state. As presented in Figure 1E and Figure S5, SAPTC@PCS and Fe-N-C@NC exhibit characteristic Fe-N peak at 399.6 eV, indicating the successful construction of Fe-N-C configuration in the single iron atom.[33,34] Meanwhile, the high-resolution XPS spectrum of Fe 2p is deconvoluted into four pairs of peaks, wherein the peaks located at 721.1/707.3 eV are correlated to Fe-C bonds, verifying the existence of Fe-N_4 and Fe_3C.[35,36] Compared with the other samples, the absence of Fe-C bonds in the XPS spectrum of Fe-N-C@NC demonstrates the absence of Fe_3C. Moreover, the proportion of Fe-N peak of samples decreases along with the calcination temperature rising (SAPTC@PCS (8.72%), Fe_3C/Fe_{low}@PCS (7.63%) and Fe_3C@PCS (~0%)), implying the reduce of Fe-N-C: Fe_3C ratio. The Fe-N peak disappeared when the temperature reached 1200 °C, suggesting nearly all Fe-N_4 configurations were converted to Fe_3C in Fe_3C@PCS. This phenomenon was consistent with the increase of Fe-C bond proportion of SAPTC@PCS (8.81%), Fe_3C/Fe_{low}@PCS (25.93%) and Fe_3C@PCS (27.4%). Subsequently, X-ray absorption near-edge structure (XANES) and extended X-ray absorption fine structure (EXAFS) spectrum of Fe K-edge were collected to clarify the

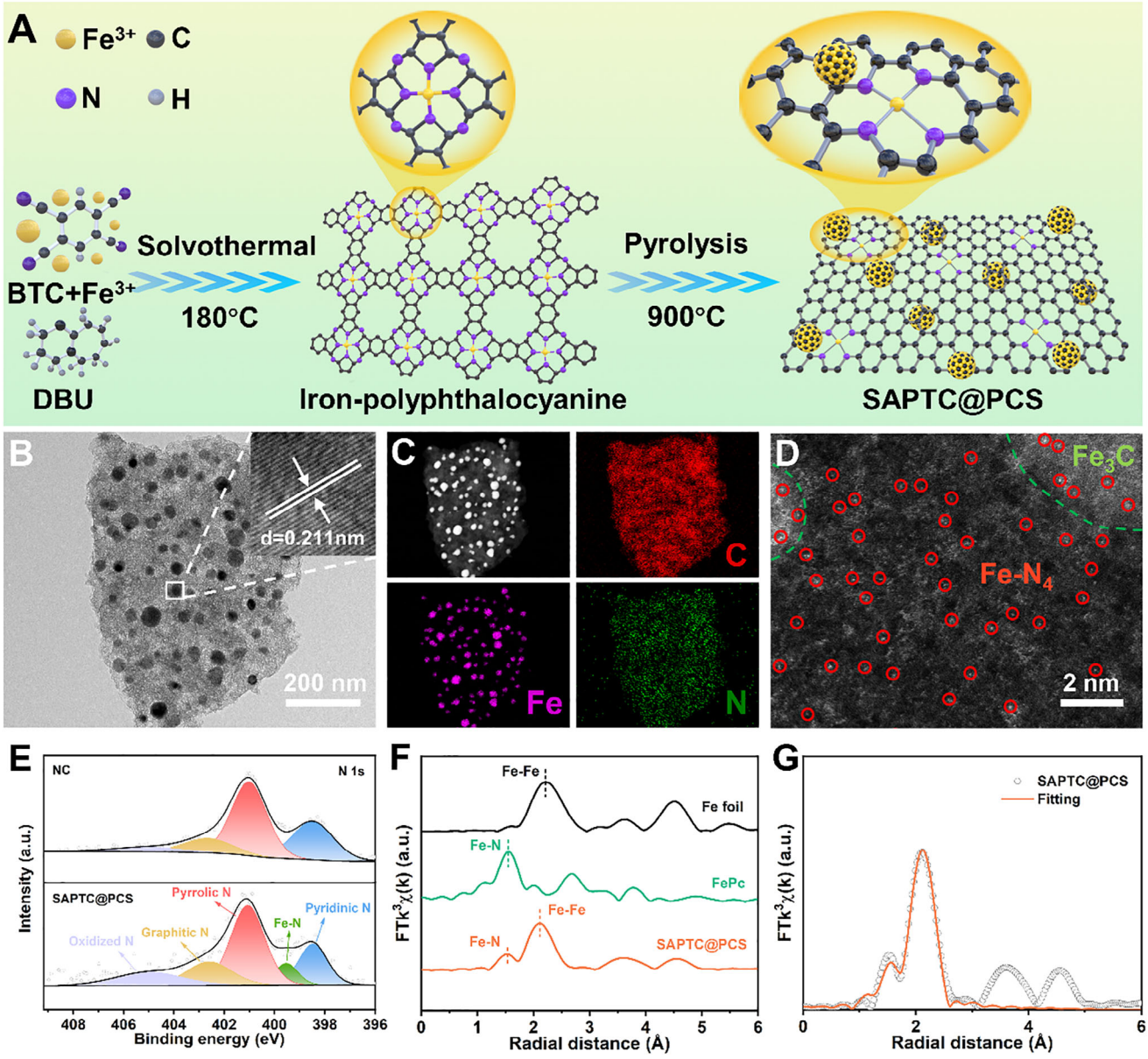

Figure 1. Schematic illustration and characterizations of SAPTC@PCS. A) Schematic illustration of the synthetic route of SAPTC@PCS. B) TEM images of SAPTC@PCS and C) the corresponding element mapping images of C, N, Fe elements. D) HAADF-STEM image of SAPTC@PCS. E) High resolution XPS spectra of N 1s for SAPTC@PCS. F) k^3-weighted FT-EXAFS curves of Fe foil, FePc and SAPTC@PCS. G) FT-EXAFS fitting curves in R space of SAPTC@PCS.

electronic structure and coordination environment (Figure S6A, Supporting Information). As exhibited in Figure 1F, the Fourier-transformed (FT) k^3-weighted EXAFS spectra of SAPTC@PCS displays an evident Fe-N peak at 1.54 Å and Fe-Fe peak (2.12 Å), respectively.[37,38] The fitting curve originated from the first shell Fe-Fe and Fe-N scattering paths is highly matched with the experimental data, and the calculated coordination number of Fe-N shell is 3.7, confirming the planar-symmetric Fe-N_4 structure in SAPTC@PCS (Figure 1G).[39] In comparison with Fe foil, the negative shifts of the Fe-N bond (-0.02 Å) and Fe-Fe bond (-0.09 Å) reflect the strong interaction between Fe_3C and Fe-N_4. The shorter bond length represents higher bond energy and stability, which endowing Fe-N_4 with reinforced catalytic activity.[27] The results of wavelet transformed EXAFS (WT-EXAFS) contour plots are highly consistent with that of FT-EXAFS (Figure S6B–D, Supporting Information).

The mechanism of tandem catalysis for fast Li^+ desolvation and sulfur conversions by adopting SAPTC@PCS is depicted in **Figure** 2A. Initially, the outer solvation shells of large $Li(solvents)_x^+$ clusters are dissociated under electrocatalysis effect, endowing the released free Li^+ with a faster diffusion kinetics to participate in the successive sulfur conversions. Simultaneously, the SAPTC@PCS performs strong adsorption and catalysis toward polysulfides, yielding dramatically improved sulfur

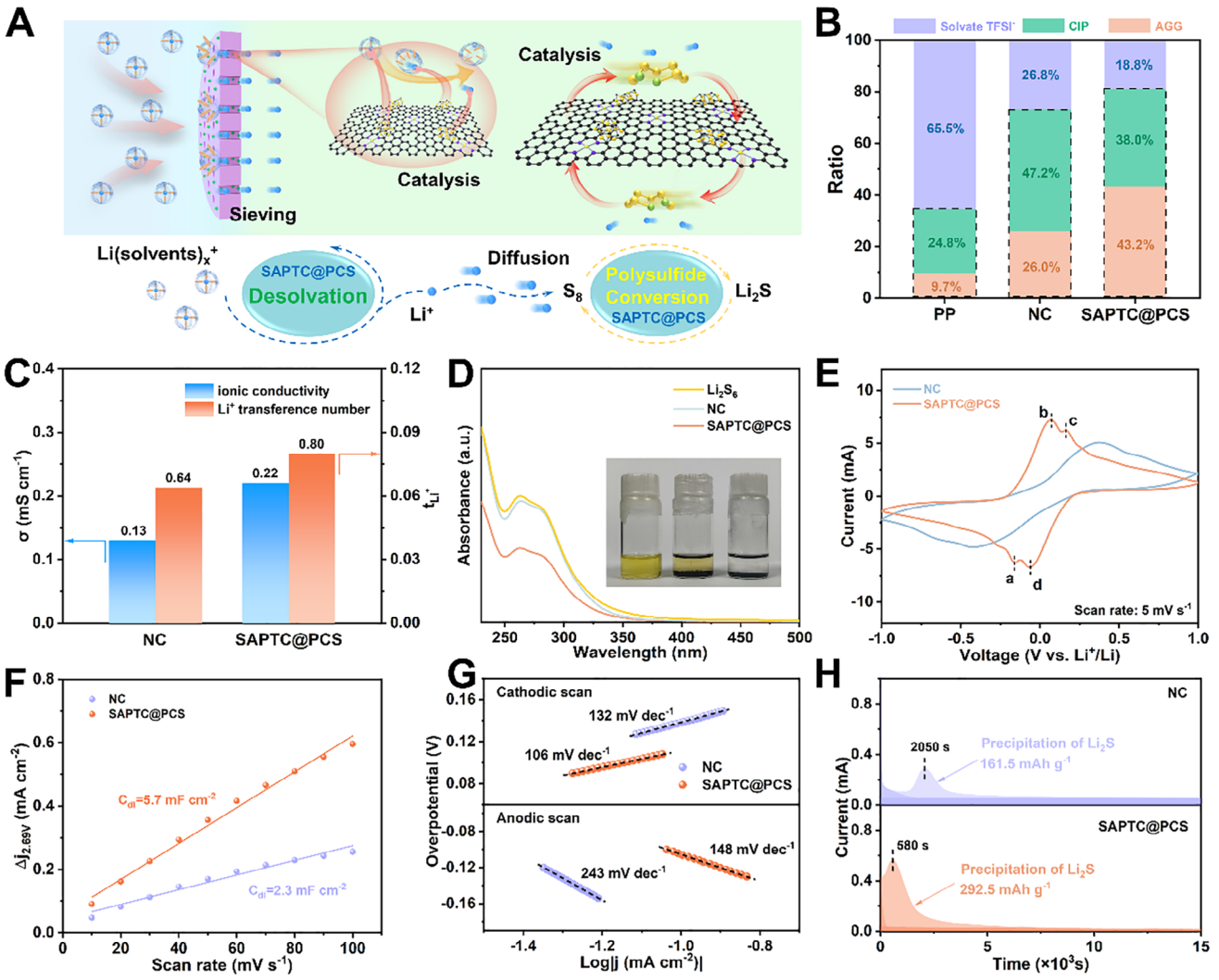

Figure 2. Tandem catalysis toward desolvation and polysulfide conversion under SAPTC@PCS accelerator. A) Schematic illustration of Li^+ desolvation process catalyzed by SAPTC@PCS. B) Ratio summary of solvate $TFSI^-$, CIP, and AGG in different systems derived from the results of Raman spectra analysis. C) Ionic conductivity and Li^+ transference number of different cells. D) Visualized adsorption experiment and UV-vis spectra of Li_2S_6 solution adsorbed by NC and SAPTC@PCS. E) CV curves of symmetric cells based on active material electrodes at 5 mV s^{-1}. F) The relation of C_{dl} currents to the scan rate at 2 .69V. G) Tafel slopes of NC and SAPTC@PCS electrodes. H) Potentiostatic discharge curves of Li_2S_8 on different electrodes at 2.05 V.

redox reactions kinetics. The Li^+ desolvation behaviors were evaluated by the ratio of contact ion pairs (CIP) and aggregates (AGGs) in different systems through Raman spectroscopy.[40,41] As presented in Figure 2B and Figure S7 (Supporting Information), the highest overall ratio of AGG+CIP (81.2%) in SAPTC@PCS system among NC (73.2%), Fe-N-C@NC (77.9%), Fe_3C@PCS (61.5%) and PP (34.5%) systems strongly indicates the favorable desolvation performance due to the rich catalytic sites and porous structure. Moreover, the reinforced Li^+ desolvation kinetics upon SAPTC@PCS is also reflected by the higher Li^+ ionic conductivity (0.22 vs 0.13 mS cm^{-1}) and transference number (0.80 vs 0.64) as shown in Figure 2C.[42,43] The faster Li^+ diffusion kinetic is surely beneficial from the catalysis and pore sieving of SAPTC@PCS. Then, the adsorption ability to polysulfides was investigated by an optical test, and the supernatant of each solution was further studied by UV-vis measurement. As shown in Figure 2D, the signal intensity decreased more significantly after the SAPTC@PCS soaking in the Li_2S_6 solution, which intuitively suggests the stronger affinity to polysulfides.[44] Subsequently, the sulfiphilicity of SAPTC@PCS is verified by XPS analysis where both terminal sulfur (S_T^{-1}) and bridging sulfur (S_B^0) peaks of Li_2S_6 exhibit an upshift to higher binding energy, reflecting the strong electron interactions between SAPTC@PCS and polysulfides.[45–47] More importantly, a new Fe-S bond at 729.6/716.2 eV is observed (Figure S8, Supporting Information), confirming the Lewis acid-base interaction between SAPTC@PCS and polysulfides, which inhibits the polysulfide shuttling and reduces their conversion barriers.[48]

To study the effect of tandem catalysis for accelerated Li^+ desolvation on sulfur redox reactions, cyclic voltammetry (CV) and electrochemical impedance spectra (EIS) were conducted

in symmetric cells. As shown in Figure 2E and Figure S9 (Supporting Information), the smallest polarization and lowest electrochemical resistance were detected in SAPTC@PCS electrode, indicating accelerated kinetics of ions diffusion for faster polysulfide conversion.[49] To evaluate the active surface area of samples, double-layer capacitance (C_{dl}) was measured (Figure S10, Supporting Information). The calculated C_{dl} value of SAPTC@PCS (5.7 mF cm^{-2}) is higher than that of NC (2.3 mF cm^{-2}), Fe_3C/Fe_{low}@PCS (4.6 mF cm^{-2}), Fe-N-C@PCS (3.3 mF cm^{-2}) and Fe_3C@PCS (2.5 mF cm^{-2}), revealing the highest catalytic active area for catalyzing the kinetics of Li^+ desolvation (Figure 2F).[30] The active area reduced with the decrease of Fe-N-C: Fe_3C ratio due to the conversion of Fe-N_4 configurations. The Tafel test is also adopted to understand the catalytic effect of SAPTC@PCS. As illustrated in Figure S11 (Supporting Information), the SAPTC@PCS electrode exhibits a higher current exchange density and lower Tafel slopes, indicating an enhanced reactions kinetics thanks to the boosted Li^+ desolvation (Figure 2G). The potentiostatic nucleation and decomposition experiments were also applied to reveal the catalytic effects of samples on the redox kinetics of liquid-solid conversion. According to Faraday's law, the SAPTC@PCS exhibited the earliest responsivity and the highest capacity, manifesting the favorable redox kinetics. (Figure 2H; Figure S12, Supporting Information). Moreover, the SEM images for the morphology of Li_2S precipitation are presented in Figure S13 (Supporting Information). As temperature increased from 0 °C to 25 °C, thicker Li_2S films were observed on both NC and SAPTC@PCS surface, indicating greater utilization of sulfur at higher operating temperature in an appropriate range. Meanwhile, it was found that the surface of SAPTC@PCS was covered by continuum Li_2S film with a higher thickness than NC at the same temperature, especially at 25 °C which displays a heterogeneous morphology, suggesting inhibited surface passivation and a higher precipitation capacity.[50]

Later, CR2032 coin-type cells were assembled to investigate the overall performance of Li-S batteries. The thermogravimetric curves in Figure S14 (Supporting Information) indicate that the sulfur content in the cathode is 61.4 wt%. As presented in Figure S15 (Supporting Information), the CV profiles of Li-S batteries exhibit characteristic cathodic and anodic peaks, corresponding to the multi-step conversion of polysulfides. Typically, the two cathodic peaks (A, B) at 2.28 and 2.02 V refer to the reduction of long chain S_8 into Li_2S, respectively, and the anodic peaks C at 2.40 V are ascribed to the oxidation process of Li_2S back to S_8. Compared with NC, the SAPTC@PCS based cells delivered higher peak intensity and smaller potential hysteresis, indicating enhanced sulfur redox kinetics and suppressed polarization. With the increase of the scan rates, the cells with SAPTC@PCS displayed smaller potential shifts of the redox peaks than that of NC, further implying their superior reaction dynamics. The fabricated cell with SAPTC@PCS-modified separator delivers an initial discharge capacity of 1030.8 mAh g^{-1} at 0.2 C (1C = 1675 mA g^{-1}) and stabilizes at 805.7 mAh g^{-1} after 150 cycles (**Figure 3A**). In contrast, the cell with NC shows much faster capacity decay. This phenomenon is further highlighted by the voltage-capacity curves in Figure S16 (Supporting Information). To further investigate the tendency of samples with different component ratios on electrochemical reactions, the galvanostatic charge/discharge (GCD) test at a current rate of 0.5 C was conducted. As illustrated in Figure S17 (Supporting Information), the cell with SAPTC@PCS delivered the smallest polarization potential (ΔE = 276 mV) in comparison with those of Fe-N-C@NC (353 mV), Fe_3C/Fe_{low}@PCS (315 mV) and Fe_3C@PCS (376 mV). Meanwhile, the ratio of Q_2/Q_1 (Q_2 and Q_1 represent the discharge capacity of the two plateaus) was also collected, where a higher Q_2/Q_1 ratio indicates the higher catalytic capability. The Q_2/Q_1 values of the cells with SAPTC@PCS (1.91) was higher than those of Fe-N-C@NC (1.67), Fe_3C/Fe_{low}@PCS (1.80) and Fe_3C@PCS (1.56). From Fe-N-C@NC to Fe_3C@PCS, the ratio of Fe-N-C: Fe_3C decreases monotonically, while the kinetics of reaction increase first and then decrease, owing to the loss of Fe single atoms and electronic redistribution between Fe-N_4 and Fe_3C. As a result, the cells based on SAPTC@PCS delivered highest discharge capacities and excellent cycle stability, indicating best electrochemical performance, which was consistent with the results of CV analysis and GCD curves (Figure S18, Supporting Information). Moreover, the SAPTC@PCS based cell shows a better rate performance, delivering 1018.9, 906.8, 811.0, 713.3 and 651.4 mAh g^{-1} at the rates of 0.2, 0.5, 1, 2 and 3 C, respectively (Figure 3B). The two distinctive discharge plateaus are well maintained with the increase of the current rate even up to 3C (Figure 3C). In comparison with NC, the cell with SAPTC@PCS separator has lower ΔE under the same rates, indicating smaller polarization and promoted redox reaction kinetics (Figure 3D).[51,52] The long-term cycling performance was also evaluated and a lower attenuation rate of 0.048% per cycle was achieved by SAPTC@PCS based cell at 1 C for 1000 cycles due to the inhibited shuttle and accelerated sulfur conversion (Figure 3E). The galvanostatic intermittent titration technique (GITT) was synchronously conducted to further describe the internal resistance during cycling (Figure S19, Supporting Information).[53] As illustrated in Figure 3F, the internal resistance of SAPTC@PCS calculated from the potential gap between closed-circuit voltage (CCV) and quasi-open-circuit voltage (QOCV) are obviously lower than NC upon the whole delithiation and lithiation process. To further pursue the practical viability of Li-S batteries, the sulfur loading was raised up to 6.0 mg cm^{-2}. Remarkably, the SAPTC@PCS-containing battery exhibited an initial discharge capacity of 1023.3 mAh g^{-1} at 0.1 C and maintained a high areal capacity of 4.59 mAh cm^{-2} after 90 cycles as shown in Figure 3G, which is much higher than that of state-of-the-art lithium-ion batteries. Furthermore, the assembled Li-S batteries based on SAPTC@PCS can energetically illuminate a light-emitting diode (LED) panel. Finally, the low-temperature (0 °C) adaptability of cell with SAPTC@PCS was studied (Figure 3H). Impressively, an outstanding capacity of 804.8 mAh g^{-1} was stably delivered after 100 cycles. These results strongly confirm the tandem catalysis of SAPTC@PCS improves the desolvation kinetics for fast conversions of sulfur species.

In situ Raman spectra technology was performed to better understand the shuttle inhibition of SAPTC@PCS on polysulfides (**Figure 4A**). As shown in Figure 4B, obvious Raman signals of various polysulfides like S_4^{2-} (202 cm^{-1}), S_6^{2-} (398 cm^{-1}) and S_5^{2-}+S_4^{2-} (454 cm^{-1}) were detected in the battery without any catalyst.[35] And these signals exist along with the entire discharge proceeds. On the contrary, the battery with SAPTC@PCS

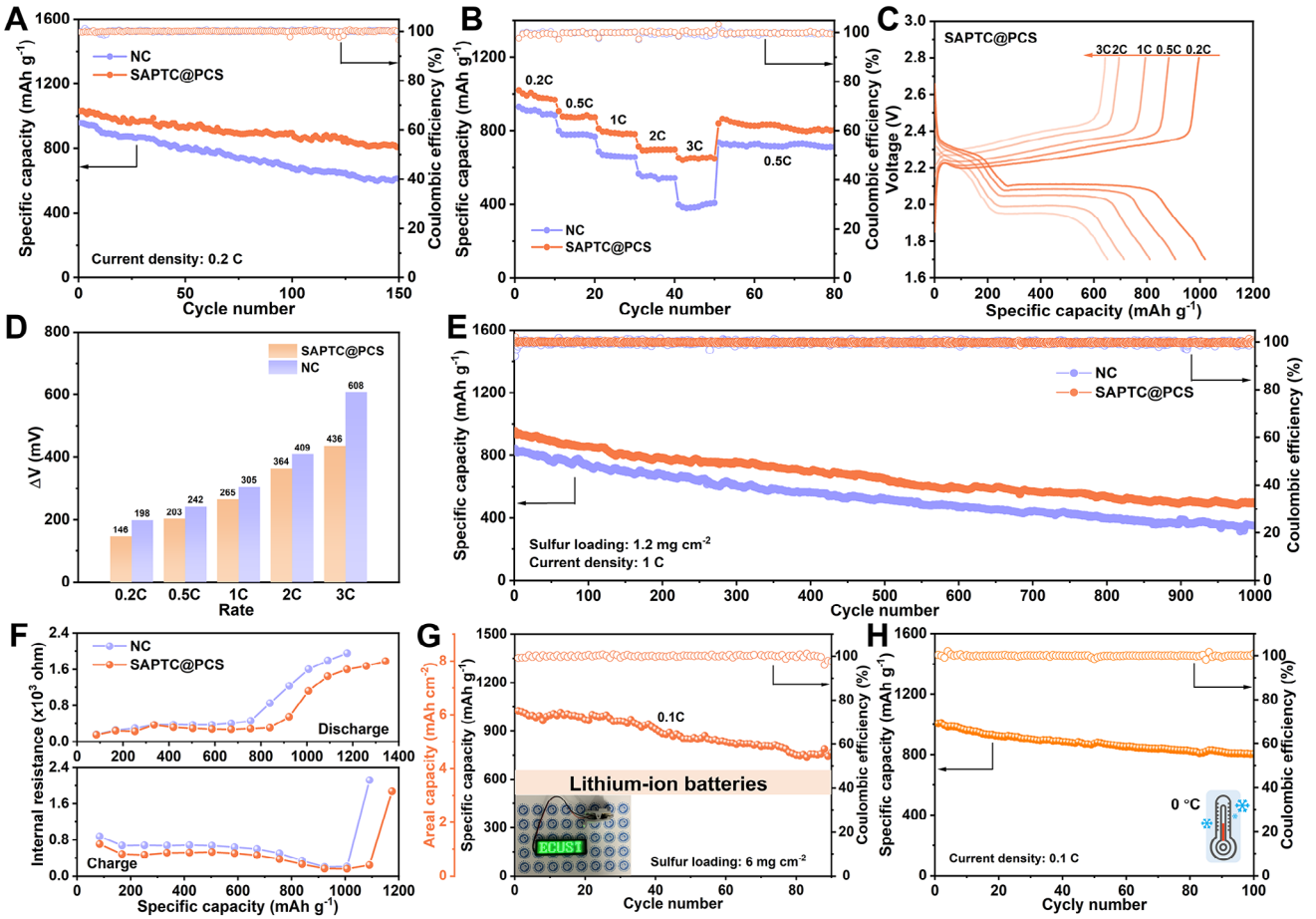

Figure 3. Electrochemical catalytic behaviors in Li-S full batteries. A) Cyclic performance of the cells at 0.2 C. B) Rate performance and C) voltage-capacity curves of the cells at different current rates. D) Polarization potential of the cells at different current rates. E) Cyclic performance at 1 C for 1000 cycles of cells based on NC and SAPTC@PCS. F) Internal resistance of cells during discharge and charge process. G) Cyclic performance of the cell with a high sulfur loading up to 6 mg cm^{-2}. H) Low-temperature (0 °C) adaptability for SAPTC@PCS modified cells.

catalyst exhibits barely Raman signals of polysulfides in addition to the peak at 482 cm^{-1} originated from the liquid electrolyte, suggesting the greatly suppressed diffusion of dissolved polysulfides. The cycled sulfur cathodes were analyzed by time-of-flight secondary-ion mass spectroscopy (TOF-SIMS) to trace the evolution and distribution of polysulfides. As presented in Figure 4C,D, the intensities of S^- or LiS^- secondary ions of SAPTC@PCS based cathode are higher than NC throughout the fully charged or discharged, respectively, which is in good agreement with the results of 2D distribution images of selected area in Figure 4E, indicating more active materials are reserved due to the strong catalytic capability of SAPTC@PCS.[54] Additionally, the 3D reconstructions of distributed S^- and LiS^- species were obtained in the SAPTC@PCS system (Figure 4F), demonstrating the higher Li^+ conductivity and more complete sulfur redox conversion.[24] The mechanism of tandem catalysis effects to boost the overall electrochemical performance in Li-S batteries is illustrated in Figure 4G. First, the SAPTC@PCS provides electrocatalytic and sieving effects to $Li(solvent)_x^+$ dissociation releasing abundant isolated Li^+. Then, the outer solvation shells of $Li(solvents)_x^+$ clusters are adsorbed and endow the released isolated Li^+ with a faster diffusion kinetics to participate in the successive sulfur conversions, contributing to lower reaction resistances, yielding much improved sulfur redox reaction kinetics and hence a desirable performance Li-S battery.

Density functional theory (DFT) and ab initio molecular dynamics (AIMD) simulations were performed to unveil enhanced desolvation behavior of Li^+ and polysulfide conversions. As shown in the electrostatic potential maps in **Figure 5**A, the Fe-N_4 system exhibits a relatively isolated electronic environment, where the area of higher electronic density (red region) is confined to the immediate vicinity of the Fe-N_4 center. In contrast, the Fe_3C cluster introduces new regions of electronic redistribution into the SAPTC@PCS system, as evidenced by the expanded electrostatic potential field around the Fe-N_4 site, which indicates enhanced electron transfer and interaction among neighboring active sites, thereby improving the catalytic performance of Fe-N_4. Figures S20–S23 (Supporting Information) display the optimized adsorption configurations of Li_2S_x (x = 8, 6, 4, 2, 1) on the surface of graphene, N-doped graphene, single atomic iron and Fe_3C, as well as the corresponding adsorption energies (E_{ads}). Apparently, whether Fe-N_4 or Fe_3C presents much higher binding energies than those of graphene and N-doped graphene to polysulfides, suggesting strong inhabitation to shuttle effect. This

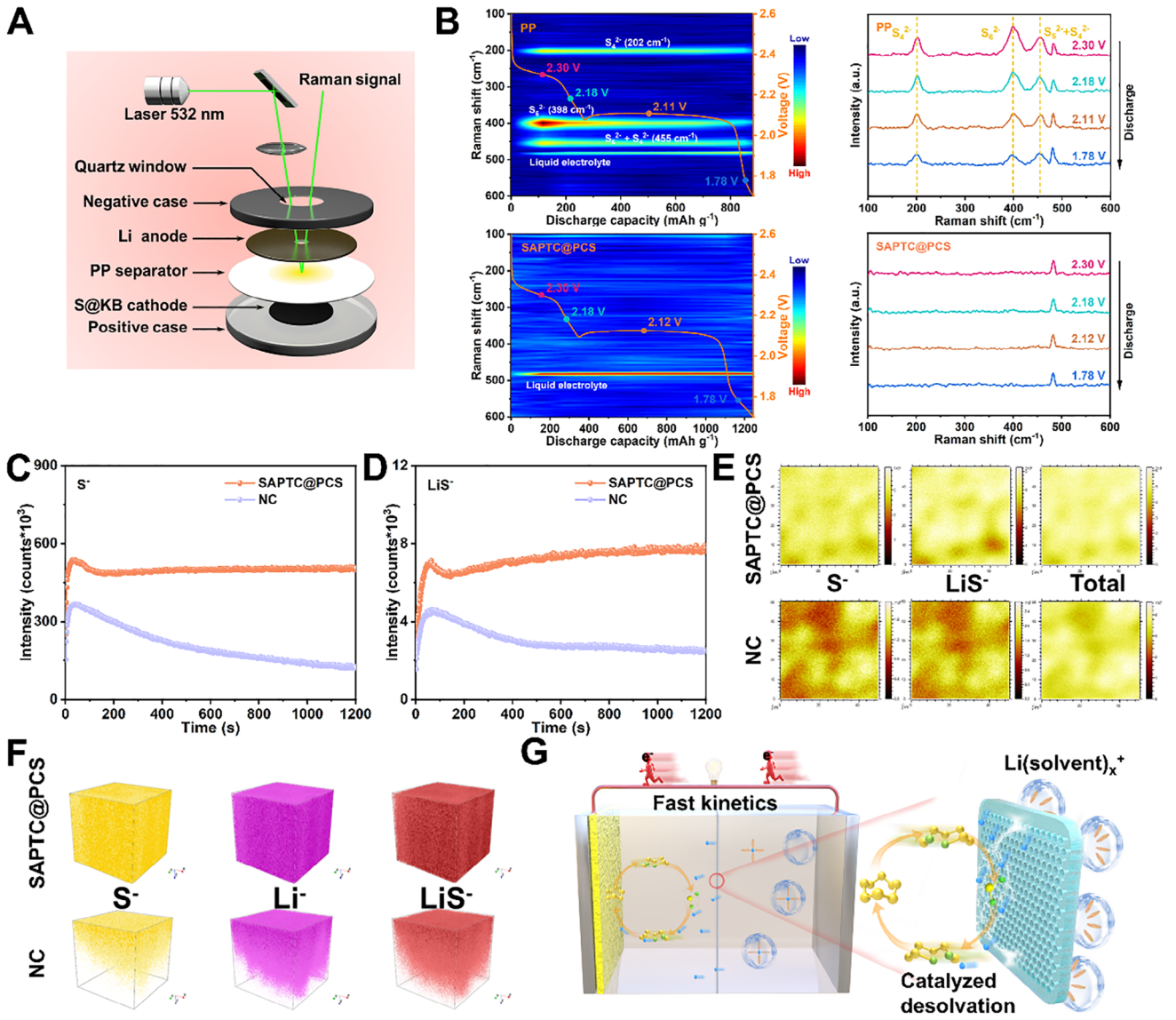

Figure 4. Catalytic mechanism probed by in situ Raman spectra and TOF-SIMS analysis. A) Schematic diagram of battery assembled for in situ Raman spectra analysis. B) In situ time-resolved Raman images of cell with/without SAPTC@PCS. C) S^- and D) LiS^- depth profiles of the cells after 10 cycles at 0.2 C. E) 2D secondary-ions distribution images, and F) 3D rendering secondary-ions depth profile images of the cycled cell with SAPTC@PCS. G) Illustrated mechanism of SAPTC@PCS to catalyze Li^+ desolvation behavior for fast sulfur redox kinetics.

phenomenon is further identified by the charge density difference before and after adsorbing Li_2S_4. As exhibited in Figure 5B, strong charge transfer was observed between Li_2S_4 and Fe-N_4 or Fe_3C, which leads to the formation of Fe-S and Li-N bonds to anchors the soluble polysulfides. Moreover, the great consumption of charge around S-S bonds in Li_2S_4 is detected, indicating the weakened S-S bonds derived from the strong chemisorption of Fe-N_4 or Fe_3C, which then reduced the energy barriers in conversion reactions. To reveal the contribution of specific atomic orbitals in SAPTC@PCS to sulfur species, the projected density of states (PDOS) after adsorbing Li_2S_4 was presented in Figure 5C. The overlap between the Fe *3d* and S *2p* orbitals is highlighted in green range, demonstrating orbital hybridization below the Fermi energy level. Snapshots of commercial electrolyte with Fe-N_4 or SAPTC@PCS via AIMD simulations are presented in Figure 5D and Figure S24 (Supporting Information). As shown in Figure 5E, the calculated radial distribution function (RDF) and coordination number (CN) peak values of Li-O in Fe-N_4 system are higher than those of SAPTC@PCS system, indicating a more stable solvation shell around Li^+ in Fe-N_4 system, which will cause the following desolvation more difficult. Moreover, the comparison of interaction energy between Li^+ and solvent at 0 °C and 25 °C in Figure 5F also demonstrates the higher Li^+ desolvation barriers in Fe-N_4 system. The relative Gibbs free energies (ΔG) of the polysulfides conversion from S_8 to Li_2S on Fe-N_4 and SAPTC@PCS were calculated. As shown in Figure 5G, the reduction of S_8 to Li_2S_8 on both samples are spontaneous exothermic conversions. In the following conversions from Li_2S_8 to Li_2S,

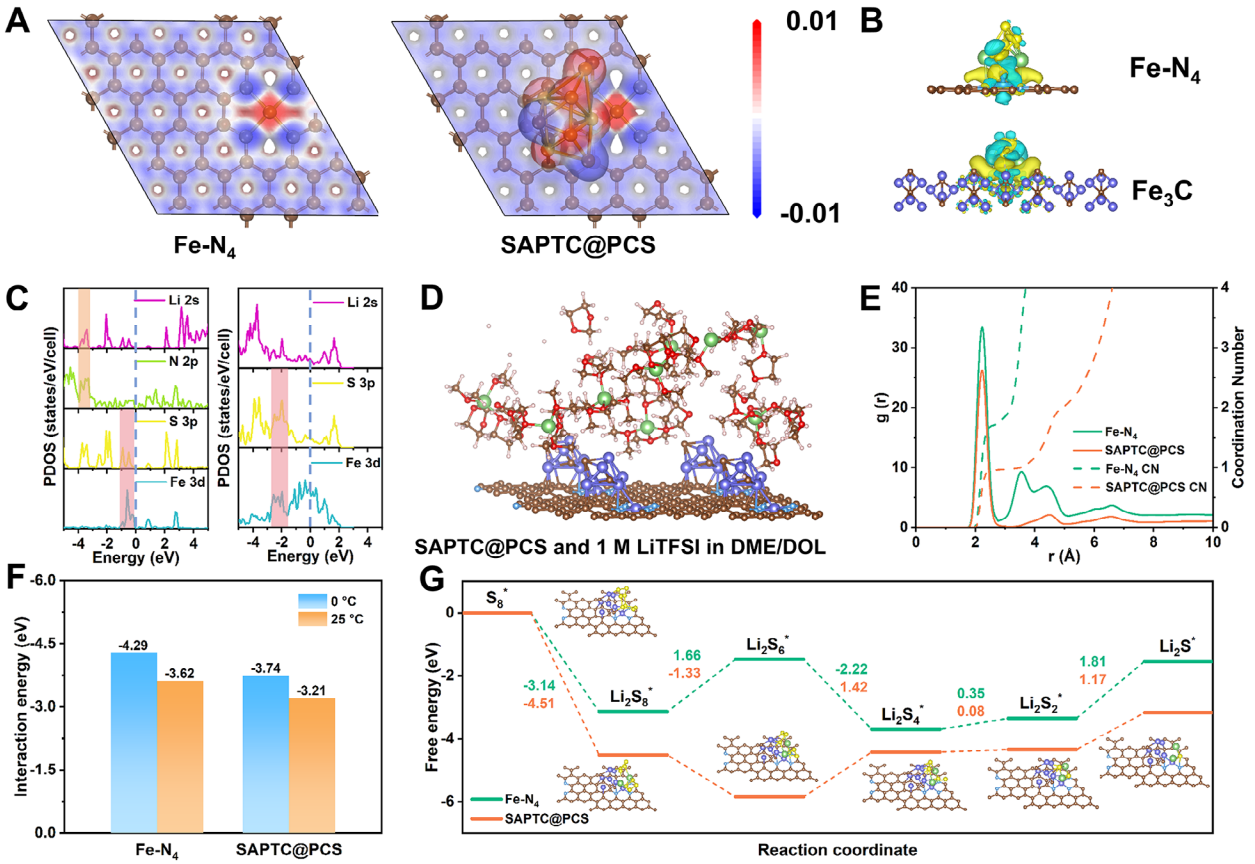

Figure 5. Theoretical studies unveiling the enhanced desolvation behavior of Li^+ and polysulfide conversions. A) The electrostatic potential maps of Fe-N_4 configuration and SAPTC@PCS. B) Charge density difference when Li_2S_4 is adsorbed on (up) Fe-N_4 and (down) Fe_3C. C) PDOS patterns of Fe-N_4 and Fe_3C adsorbed by Li_2S_4. D) Snapshot of commercial electrolyte with SAPTC@PCS via AIMD simulations. E) The radial distribution function and coordination number peak values of Li-O in the commercial electrolyte with the presence of Fe-N_4 and SAPTC@PCS. F) Interaction energy between Li^+ and solvent molecules in the commercial electrolyte at different temperatures. G) Gibbs free energy curves for the conversion of LiPSs.

SAPTC@PCS delivers a lower ΔG (1.34 eV) than that on Fe-N_4 (1.60 eV), indicating that the reduction of polysulfides is more favorable on the SAPTC@PCS.

3. Conclusion

In summary, the tandem catalyst consisted of single Fe atom and Fe_3C nanoparticles on porous carbon sheet is initially proposed and developed as Li^+ desolvation promoter in Li-S batteries. As revealed by as revealed by theoretical simulation, in situ Raman, time-of-flight second ion mass spectroscopy, electronic microscope and X-ray measurements, the as-prepared SAPTC@PCS facilitates the dissociation of $Li(solvent)_x^+$ to release more isolated Li^+ to participate in the subsequent polysulfide redox conversions by decreasing the related barriers, contributing to fast kinetics of Li^+ diffusion and sulfur redox reactions. Consequently, the cell with SAPTC@PCS delivers a high rate performance at 3 C and long-term cycling performance up to 1000 cycles. Impressively, the cell employed with 6 mg cm^{-2} stabilizes the capacity of 4.59 mAh cm^{-2} after 90 cycles, and a desirable capacity of 804.8 mAh g^{-1} after 100 cycles is achieved even being exposed to low temperature of 0 °C. This work highlights the significance of interfacial Li^+ desolvation, and demonstrates the feasibility of single atom-particle catalysts for tandem catalysis in Li-S batteries.

Supporting Information

Supporting Information is available from the Wiley Online Library or from the author.

Acknowledgements

This work was financially supported by the National Natural Science Foundation of China (No. 52372045, 22075081, 21972164, 22279161, 12264038, 22309144 and U1710252), National Key R&D Program of China (2021YFA1201503), the Natural Science Foundation of Jiangsu Province (BK. 20210130), the Fundamental Research Funds for the Central Universities (JKD01231701), China Postdoctoral Science Foundation (No. 2023M731084; 2024M762318), Shanghai Sailing Program of China (23YF1408900); and Opening funding from Key Laboratory of Engineering Dielectrics and Its Application (Harbin University of Science and Technology) (No. KFM202507, Ministry of Education). J.W. also acknowledges the funding provided by the Alexander von Humboldt Foundation and the basic funding of the Helmholtz Association. Y.Z. thanks the Shanghai Super Postdoctoral Incentive Program. The authors thank the Research Center of Analysis and Test of East China University of Science and Technology

for the assistance with the characterization. The authors also thank the technical support from Nano-X, Suzhou Institute of Nano-tech and Nano-bionics, Chinese Academy of Sciences.

Open access funding enabled and organized by Projekt DEAL.

Conflict of Interest

The authors declare no conflict of interest.

Data Availability Statement

The data that support the findings of this study are available from the corresponding author upon reasonable request.

Keywords

desolvation behavior, lithium-sulfur batteries, single-atom catalysts, sulfur conversions, tandem catalysis

Received: January 16, 2025
Revised: March 22, 2025
Published online:

[1] J. Gu, Y. Shi, Z. Du, M. Li, S. Yang, *Adv. Energy Mater.* **2023**, *13*, 2302091.
[2] B. Hu, J. Xu, Z. Fan, C. Xu, S. Han, J. Zhang, L. Ma, B. Ding, Z. Zhuang, Q. Kang, X. Zhang, *Adv. Energy Mater.* **2023**, *13*, 2203540.
[3] J. Xu, Y. Yang, A. Zhu, Y. Wang, B. Peng, L. Ma, Y. Cao, Y. Wang, *Chem. Eng. J.* **2024**, *487*, 150527.
[4] H. Chen, Z. Cao, J. Gu, Y. Cui, Y. Zhang, Z. Zhao, Z. Cheng, Q. Zhao, B. Li, S. Yang, *Adv. Energy Mater.* **2021**, *11*, 2003746.
[5] Z. Zheng, X. Zhong, Q. Zhang, M. Zhang, L. Dai, X. Xiao, J. Xu, M. Jiao, B. Wang, H. Li, Y. Jia, R. Mao, G. Zhou, *Nat. Commun.* **2024**, *15*, 753.
[6] F. Cao, X. Zhang, Z. Jin, J. Zhang, Z. Tian, D. Kong, Y. Li, Y. Li, L. Zhi, *Adv. Energy Mater.* **2024**, *14*, 2303893.
[7] G. Zhou, H. Chen, Y. Cui, *Nat. Energy* **2022**, *7*, 312.
[8] C. Dong, C. Ma, C. Zhou, Y. Yu, J. Wang, K. Yu, C. Shen, J. Gu, K. Yan, A. Zheng, M. Gong, X. Xu, L. Mai, *Adv. Mater.* **2024**, *36*, 2407070.
[9] Q. Zhang, Z. Zheng, R. Gao, X. Xiao, M. Jiao, B. Wang, G. Zhou, H. M. Cheng, *Adv. Mater.* **2024**, *36*, 2401018.
[10] H. Zhang, J. Chen, Z. Li, Y. Peng, J. Xu, Y. Wang, *Adv. Funct. Mater.* **2023**, *33*, 2304433.
[11] C. Zhou, C. Dong, W. Wang, Y. Tian, C. Shen, K. Yan, L. Mai, X. Xu, *Interdiscip. Mater.* **2024**, *3*, 306.
[12] W. Qu, Z. Lu, C. Geng, L. Wang, Y. Guo, Y. Zhang, W. Wang, W. Lv, Q. H. Yang, *Adv. Energy Mater.* **2022**, *12*, 2202232.
[13] J. Wang, H. Liu, J. Zhang, Q. Xiao, C. Wang, Y. Zhang, M. Liu, Q. Kang, L. Jia, D. Wang, Q. Li, W. Duan, H. Adenusi, S. Passerini, Y. Zhang, H. Lin, *Energy Storage Mater.* **2024**, *67*, 103289.
[14] C. Zhao, Y. Huang, B. Jiang, Z. Chen, X. Yu, X. Sun, H. Zhou, Y. Zhang, N. Zhang, *Adv. Energy Mater.* **2023**, *14*, 2302586.
[15] X. Zhang, Z. Ni, X. Bai, H. Shen, Z. Wang, C. Wei, K. Tian, B. Xi, S. Xiong, J. Feng, *Adv. Energy Mater.* **2023**, *13*, 2301349.
[16] Z. Yu, X. Huang, M. Zheng, S.-Q. Zhang, Y. Yang, J. Lu, *Adv. Mater.* **2023**, *35*, 2300861.
[17] J. Xu, H. Zhang, F. Yu, Y. Cao, M. Liao, X. Dong, Y. Wang, *Angew. Chem., Int. Ed.* **2022**, *61*, 202211933.
[18] X. Zhang, X. Li, Y. Zhang, X. Li, Q. Guan, J. Wang, Z. Zhuang, Q. Zhuang, X. Cheng, H. Liu, J. Zhang, C. Shen, H. Lin, Y. Wang, L. Zhan, L. Ling, *Adv. Funct. Mater.* **2023**, *33*, 2302624.
[19] Y. Zhang, C. Kang, W. Zhao, Y. Song, J. Zhu, H. Huo, Y. Ma, C. Du, P. Zuo, S. Lou, G. Yin, *J. Am. Chem. Soc.* **2023**, *145*, 1728.
[20] J. Wang, J. Zhang, J. Wu, M. Huang, L. Jia, L. Li, Y. Zhang, H. Hu, F. Liu, Q. Guan, M. Liu, H. Adenusi, H. Lin, S. Passerini, *Adv. Mater.* **2023**, *35*, 2302828.
[21] J. Zhang, R. He, Q. Zhuang, X. Ma, C. You, Q. Hao, L. Li, S. Cheng, L. Lei, B. Deng, X. Li, H. Lin, J. Wang, *Adv. Sci.* **2022**, *9*, 202202244.
[22] J. Wang, L. Jia, S. Duan, H. Liu, Q. Xiao, T. Li, H. Fan, K. Feng, J. Yang, Q. Wang, M. Liu, J. Zhong, W. Duan, H. Lin, Y. Zhang, *Energy Storage Mater.* **2020**, *28*, 375.
[23] Z. Han, S. Zhao, J. Xiao, X. Zhong, J. Sheng, W. Lv, Q. Zhang, G. Zhou, H.-M. Cheng, *Adv. Mater.* **2021**, *33*, 2105947.
[24] L. Ren, K. Sun, Y. Wang, A. Kumar, J. Liu, X. Lu, Y. Zhao, Q. Zhu, W. Liu, H. Xu, X. Sun, *Adv. Mater.* **2024**, *36*, 2310547.
[25] J. Wang, J. Zhang, Y. Zhang, H. Li, P. Chen, C. You, M. Liu, H. Lin, S. Passerini, *Adv. Mater.* **2024**, *36*, 2402792.
[26] L.-J. Yuan, B. Liu, L.-X. Shen, Y.-K. Dai, Q. Li, C. Liu, W. Gong, X.-L. Sui, Z.-B. Wang, *Adv. Mater.* **2023**, *35*, 2305945.
[27] L. Li, Y. Wen, G. Han, F. Kong, L. Du, Y. Ma, P. Zuo, C. Du, G. Yin, *SmallSmall* **2023**, *19*, 2300758.
[28] M. Karuppannan, J. E. Park, H. E. Bae, Y.-H. Cho, O. J. Kwon, *NanoscaleNanoscale* **2020**, *12*, 2542.
[29] H. Gong, H. Xue, M. Yue, X. Yu, S. Zhang, T. Wang, J. He, *Chem. Eng. J.* **2024**, *480*, 147985.
[30] H. Li, J. Wang, T. Tjardts, I. Barg, H. Qiu, M. Müller, J. Krahmer, S. Askari, S. Veziroglu, C. Aktas, L. Kienle, J. Benedikt, *Small* **2024**, 2310660.
[31] H. Zhu, Q. Liu, S. Cao, H. Chen, Y. Liu, *Small* **2023**, *20*, 2308136.
[32] G. Li, W. Qiu, W. Gao, Y. Zhu, X. Zhang, H. Li, Y. Zhang, X. Wang, Z. Chen, *Adv. Funct. Mater.* **2022**, *32*, 2202853.
[33] J. Hu, C. Su, R. Li, B. Li, Z. Hou, Y. Fan, Y. Pan, J. Liu, A. Hu, *J. Alloy. Compd.* **2024**, *976*, 173146.
[34] Y. Ding, T. Yan, J. Wu, M. Tian, M. Lu, C. Xu, J. Gu, H. Zhao, Y. Wang, X. Pan, S. X. Dou, L. Zhang, J. Sun, *Appl. Catal. B* **2024**, *343*, 123553.
[35] X. Zhou, Y. Cui, X. Huang, Q. Zhang, B. Wang, S. Tang, *Chem. Eng. J.* **2023**, *457*, 141139.
[36] J. Wang, L. Jia, H. Liu, C. Wang, J. Zhong, Q. Xiao, J. Yang, S. Duan, K. Feng, N. Liu, W. Duan, H. Lin, Y. Zhang, *ACS Appl. Mater. Interfaces* **2020**, *12*, 12727.
[37] H. Chen, Y. Wang, S. Zhang, Y. He, L. Hou, C. Yuan, *Chem. Eng. J.* **2024**, *479*, 147422.
[38] J. Wang, L. Jia, J. Zhong, Q. Xiao, C. Wang, K. Zang, H. Liu, H. Zheng, J. Luo, J. Yang, H. Fan, W. Duan, Y. Wu, H. Lin, Y. Zhang, *Energy Storage Mater.* **2019**, *18*, 246.
[39] L. Yang, X. Wang, X. Cheng, Y. Zhang, C. Ma, Y. Zhang, J. Wang, W. Qiao, L. Ling, *Adv. Funct. Mater.* **2023**, *33*, 2303705.
[40] L. Li, H. Tu, J. Wang, M. Wang, W. Li, X. Li, F. Ye, Q. Guan, F. Zhu, Y. Zhang, Y. Hu, C. Yan, H. Lin, M. Liu, *Adv. Funct. Mater.* **2023**, *33*, 2212499.
[41] S. Yang, A. Chen, Z. Tang, Z. Wu, P. Li, Y. Wang, X. Wang, X. Jin, S. Bai, C. Zhi, *Energy Environ. Sci.* **2024**, *17*, 1095.
[42] J. Xu, S. An, X. Song, Y. Cao, N. Wang, X. Qiu, Y. Zhang, J. Chen, X. Duan, J. Huang, W. Li, Y. Wang, *Adv. Mater.* **2021**, *33*, 2105178.
[43] Q. Kang, Z. Zhuang, Y. Liu, Z. Liu, Y. Li, B. Sun, F. Pei, H. Zhu, H. Li, P. Li, Y. Lin, K. Shi, Y. Zhu, J. Chen, C. Shi, Y. Zhao, P. Jiang, Y. Xia, D. Wang, X. Huang, *Adv. Mater.* **2023**, *35*, 2303460.
[44] F. Zhang, Z. Tang, L. Zheng, T. Zhang, M. Xu, H. Xiao, H. Zhuang, P. Han, Q. Gao, *Appl. Catal. B* **2023**, *334*, 122876.
[45] D. Han, L. Sun, Z. Li, W. Qin, L. Zhai, Y. Sun, S. Tang, Y. Fu, *Energy Storage Mater.* **2024**, *65*, 103143.
[46] J. Xu, W. Tang, C. Yang, I. Manke, N. Chen, F. Lai, T. Xu, S. An, H. Liu, Z. Zhang, Y. Cao, N. Wang, S. Zhao, D. Niu, R. Chen, *ACS Energy Lett.* **2021**, *6*, 3053.

[47] H. Li, G. Chen, K. Zhang, L. Wang, G. Li, *Adv. Sci.* **2023**, *10*, 2303830.
[48] S. Zhang, Y. Zhang, L. Ma, C. Ma, C. Zhang, Y. Chen, L. Chen, L. Zhou, W. Wei, *SmallSmall* **2023**, *19*, 2300293.
[49] Q. Kang, Z. Zhuang, Y. Li, Y. Zuo, J. Wang, Y. Liu, C. Shi, J. Chen, H. Li, P. Jiang, X. Huang, *Nano Res.* **2023**, *16*, 9240.
[50] Z. Liu, P. P. Mukherjee, *ACS Appl. Mater. Interfaces* **2017**, *9*, 5263.
[51] H. Wang, H. Yuan, W. Wang, X. Wang, J. Sun, J. Yang, X. Liu, Q. Zhao, T. Wang, N. Wen, Y. Gao, K. Song, D. Chen, S. Wang, Y.-W. Zhang, J. Wang, *Adv. Mater.* **2023**, *36*, 2307741.
[52] J. Sheng, Q. Zhang, C. Sun, J. Wang, X. Zhong, B. Chen, C. Li, R. Gao, Z. Han, G. Zhou, *Adv. Funct. Mater.* **2022**, *32*, 2203272.
[53] Z. Kong, Y. Lin, J. Hu, Y. Wang, L. Zhan, *Chem. Eng. J.* **2022**, *436*, 132719.
[54] B. Yue, L. Wang, N. Zhang, Y. Xie, W. Yu, Q. Ma, J. Wang, G. Liu, X. Dong, *SmallSmall* **2023**, *20*, 2308603.